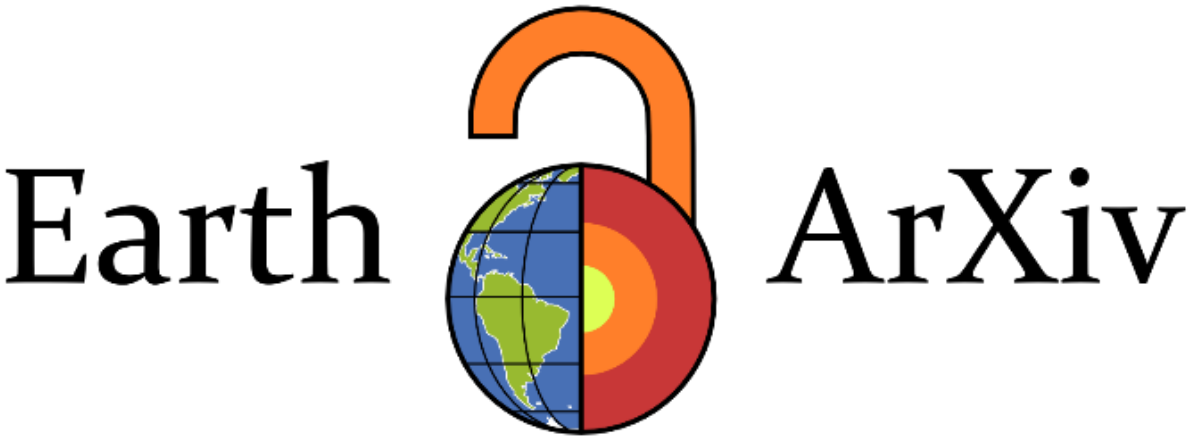

Future Strengthening of North Atlantic Anthropogenic Carbon Transport Despite AMOC Weakening

Ce Bian[1], Galen A. McKinley[1,2], Peter J. Brown[3], Elaine L. McDonagh[3,4]

[1]Lamont-Doherty Earth Observatory, Columbia University, New York, USA.
[2]Department of Earth and Environmental Sciences, Columbia University, New York, USA.
[3]National Oceanography Centre, Southampton, UK.
[4]NORCE, Norwegian Research Centre, Bjerknes Centre for Climate Research, Bergen, Norway.

Key Points:

- The CMIP6 ensemble reproduces the magnitude and variability of anthropogenic carbon transport across 26.5°N, in close agreement with observations during 2004-2012.
- Despite AMOC decline through 2100 in CMIP6 models, northward anthropogenic carbon transport strengthens due to rising upper ocean concentrations that follow emission pathways.
- The forced signal in anthropogenic carbon transport emerges within 30 years; current observations are approaching, but have not yet reached, robust detectability.

Corresponding author: Ce Bian, cebian@ldeo.columbia.edu

Abstract

The North Atlantic is a major hotspot for the uptake, accumulation, and storage of anthropogenic carbon (C_{anth}), processes that are closely linked to the Atlantic Meridional Overturning Circulation (AMOC). However, the role of ocean transport in driving this accumulation remains poorly constrained, leading to uncertainty in future carbon uptake and circulation changes under climate forcing. CMIP6 models reasonably reproduce observed C_{anth} transport at RAPID-MOCHA (26.5°N in the North Atlantic). Our results show that northward C_{anth} transport increases under SSP1-2.6, SSP2-4.5, and SSP5-8.5, despite a concomitant weakening of AMOC-related volume transport. This strengthening occurs because increases in C_{anth} concentration outweigh reductions in circulation strength. The western boundary current serves as the primary pathway for northward C_{anth} transport and is particularly sensitive to future change. A time-of-emergence analysis indicates that trends in C_{anth} transport become detectable within approximately 25–35 years, with earlier emergence under higher-emission scenarios. The RAPID observational record, that began in 2004, is approaching the detectability threshold for C_{anth} transport trends, but it remains too short to robustly resolve long-term changes in AMOC strength, whose emergence timescale is substantially longer.

1 Plain Language Summary

The Atlantic Ocean plays a major role in storing carbon released by human activities. In this study, we show that climate models successfully capture present-day carbon transport observed by the RAPID-MOCHA array at 26.5°N, providing confidence in their ability to assess how this transport may change in the future. We find that even though the Atlantic overturning circulation is expected to weaken as the climate warms, the northward movement of human-derived carbon will continue to increase. This happens because the amount of carbon dissolved in seawater rises faster than the circulation slows, a process we call circulation-concentration compensation. The western boundary current acts as the main route carrying this carbon northward and is especially sensitive to future changes. Detecting human-driven changes in anthropogenic carbon transport requires 25-35 years of observations, which the RAPID array is approaching but has not yet reached.

2 Introduction

The global carbon cycle regulates atmospheric CO_2 through exchanges among the atmosphere, ocean, land, and biosphere, mediated by physical, chemical, and biological processes (Friedlingstein et al., 2025; IPCC, 2021; IPCC, 2023). Since the Industrial Era, anthropogenic emissions have increased atmospheric CO_2 to roughly 1.5 times its pre-industrial level (Friedlingstein et al., 2025). Approximately 29% of emitted carbon is currently absorbed by the ocean, making ocean uptake a primary regulator of long-term atmospheric CO_2 accumulation (Friedlingstein et al., 2025). The oceanic uptake of anthropogenic carbon (C_{anth}) is currently due to physical and chemical mechanisms: air–sea CO_2 exchange imprints the anthropogenic signal at the surface, while ocean circulation redistributes this signal laterally and vertically into the ocean interior (Khatiwala et al., 2013; McKinley et al., 2020). As a result, the storage and redistribution of C_{anth} are tightly coupled to ocean circulation.

The North Atlantic plays a disproportionately large role in this system. Although it comprises only about 15% of the global ocean surface area, it accounts for roughly one quarter of global oceanic CO_2 uptake and contains the highest column inventories of C_{anth} worldwide (Sabine et al., 2004; Gruber et al., 2009, 2019). This efficiency is linked to the Atlantic Meridional Overturning Circulation (AMOC), where surface waters equilibrate atmospheric CO_2 as warm surface waters move northward and cool. When these waters are subducted to depth, C_{anth} is sequestered on centennial to millennial timescales (Macdonald et al., 2003; DeVries, 2014; Khatiwala et al., 2009). From a basin-scale perspective, changes

in North Atlantic anthropogenic carbon inventory reflect a balance between local air–sea CO_2 fluxes and lateral transport across basin boundaries. Quantifying advective C_{anth} fluxes from observations and using these estimates to validate Earth system models provides a valuable opportunity to assess how well models represent integrated carbon transport processes, and to evaluate their credibility in projecting future climate states.

Under continued anthropogenic forcing, the AMOC is projected to weaken over the twenty-first century (Weijer, Sijp, et al., 2020; IPCC, 2021), potentially altering the pathways and efficiency of C_{anth} redistribution. A weaker overturning circulation could reduce northward volume transport and limit deep sequestration. At the same time, rising atmospheric CO_2 increases upper-ocean C_{anth} concentrations, potentially enhancing advective carbon fluxes even if circulation strength declines. These competing influences introduce uncertainty regarding the future evolution of C_{anth} transport in the North Atlantic. Observational constraints from the RAPID–MOCHA array at 26.5°N provide valuable insight into present-day transport and its variability (McCarthy et al., 2015, 2025; Brown et al., 2021). Earth System Models allow for estimation of how circulation and concentration changes may jointly shape future C_{anth} transport, provided that they can reproduce this observed transport magnitude and variability.

Here, we evaluate CMIP6 simulations of C_{anth} transport across the subtropical North Atlantic by benchmarking model performance against RAPID-based estimates for 2004–2012 (Brown et al., 2021). We then assess projected changes under multiple SSP scenarios and decompose transport into overturning and horizontal components to isolate the relative roles of circulation strength and concentration increases. This process-based framework allows us to examine whether and why anthropogenic carbon transport may strengthen despite a weakening AMOC, and to clarify the evolving dynamical linkage between ocean circulation and carbon sequestration in a warming climate.

3 Data and Methods

3.1 Observations: RAPID–Argo array

We use gridded 10-day observational products at 26.5° N from the RAPID–MOCHA–WBTS array, together with Argo-based estimates of anthropogenic carbon (C_{anth}), for 2004–2012, following Brown et al. (2021). The RAPID gridded products optimally interpolate temperature and salinity observations from Argo profiling floats and moored sensors onto a 0.25° longitude × 20 dbar grid in the upper 1,760 dbar (Moat et al., 2026). Below 1,760 dbar, hydrographic properties were linearly interpolated between boundary moorings, while abyssal layers beneath the deepest instruments were reconstructed by extrapolating structures from repeat hydrographic sections.

C_{anth} concentrations were estimated by applying a back-calculation approach (Gruber et al., 1996) to local hydrographic data from GLODAPv2.2023 (Lauvset et al., 2023). These estimates were first detrended before regional, water-mass-specific regressions for C_{anth} were constructed using temperature and salinity as predictors. The resulting regressions were then mapped onto the 10-day gridded RAPID temperature and salinity fields, after which the trends were reintroduced. Further details on the observational C_{anth} reconstruction and data treatment are provided in Brown et al. (2021), while additional information on the RAPID–MOCHA–WBTS array is available from the RAPID project (`https://rapid.ac.uk/`).

3.2 Models: CMIP6 simulations

We analyze CMIP6 models that provide both the concentration of total DIC (Dissolved inorganic carbon, DIC_{total}) and natural DIC (DIC_{nat}), allowing explicit calculation of C_{anth} as follows:

$$C_{anth} = DIC_{total} - DIC_{nat}. \quad (1)$$

In these experiments, DIC_{nat} is obtained by running an additional tracer in the models that responds to a constant atmospheric pCO_2 (284 ppm), thus isolating the natural carbon cycle (Goris et al., 2018). DIC_{total} is obtained by running the models under the historically observed or future projected atmospheric pCO_2. Only CanESM (Swart et al., 2019a,b; Sigmond et al., 2023) and CESM2 (Danabasoglu et al., 2020) provide these tracers together for historical simulations and the SSP1-2.6, SSP2-4.5, and SSP5-8.5 scenarios, representing low-, intermediate-, and high-emission pathways, respectively. This model selection is therefore constrained by tracer availability rather than by AMOC characteristics. Nevertheless, because the subsequent analysis examines the relationship between AMOC strength and C_{anth} transport, we note that this relationship should be interpreted within the limited model availability rather than as a constraint across the full CMIP6 ensemble. There are 35 members of CanESM with historical simulations, each with 45 vertical levels, and 20 members of CESM2 with 60 vertical levels. For the historical period (1850-2014), all 55 realizations provide monthly outputs, which are regridded onto a common $1^\circ \times 1^\circ$ horizontal grid.

For consideration of future change in C_{anth} transport, we use SSP scenarios in CMIP6. For the period 2015-2100, the monthly outputs required for C_{anth} concentrations are available from only a single CanESM realization (r1i1p2f1). In contrast, yearly outputs of DIC_{total} and DIC_{nat} are available from 13 (SSP1-2.6), 15 (SSP2-4.5), and 13 (SSP5-8.5) experiments respectively.Velocity fields are available at monthly resolution, and after matching tracer and velocity availability, 7, 14, and 7 ensemble members are retained for SSP1-2.6, SSP2-4.5, and SSP5-8.5, respectively. Details of all datasets are provided in Supplementary Table 1.

To ensure consistency between the historical period (2004-2014) and future projections (2015-2100), yearly C_{anth} concentrations are linearly interpolated to monthly resolution between adjacent years. This approach is justified by the weak seasonal variability and near-linear evolution of C_{anth} on interannual timescales (Fig. S1a). C_{anth} transports derived from direct monthly output agree closely with that reconstructed from yearly output at monthly resolution (Fig. S1b), with relative errors generally below 0.1%. Therefore, although the interpolation introduces a small approximation, it does not materially affect the calculation of C_{anth} transport.

3.3 Overturning and Horizontal C_{anth} Transports

We compute the meridional C_{anth} transport across the 26.5° N section of the model fields with the same approach as has been applied to observations at RAPID (Brown et al., 2021). Let x denote the longitude along the RAPID profile and z be the depth. The instantaneous total flux is defined as the zonal–vertical integral of the product between meridional velocity and concentration, with northward transport taken as positive.

$$T_{total} \;=\; \iint v(x,z)\; C_{\mathrm{anth}}(x,z)\; dx\, dz, \tag{2}$$

To diagnose the dynamical pathways, we decompose the flux into an overturning component and a horizontal component following the RAPID convention. At each depth z, define zonal means $\overline{v}(z) = L^{-1}\int v\, dx$ and $\overline{C}_{\mathrm{anth}}(z) = L^{-1}\int C_{\mathrm{anth}}\, dx$, where L is the trans-basin distance along RAPID, and deviations $v' = v - \overline{v}$, $C'_{\mathrm{anth}} = C_{\mathrm{anth}} - \overline{C}_{\mathrm{anth}}$. Zonal integration of the product vC_{anth} then separates as

$$T_{\mathrm{total}} \;=\; T_{\mathrm{over}} \;+\; T_{\mathrm{horiz}},$$

$$T_{\mathrm{over}} \;=\; \int \overline{v}(z)\, \overline{C}_{\mathrm{anth}}(z)\, dz, \qquad T_{\mathrm{horiz}} \;=\; \iint v'(x,z)\, C'_{\mathrm{anth}}(x,z)\, dx\, dz, \tag{3}$$

because the cross terms $\int \overline{v}\, C'_{\mathrm{anth}}\, dx$ and $\int v'\, \overline{C}_{\mathrm{anth}}\, dx$ vanish in the zonal mean. Physically, T_{over} isolates the large-scale meridional overturning contribution associated with zonally co-

herent shear, while T_{horiz} captures the covariance between lateral velocity and concentration anomalies related to the gyre including the structure of the boundary-current.

3.4 Definition of AMOC strength

The AMOC strength is diagnosed from the meridional overturning streamfunction at 26.5°N. The streamfunction $\Psi(z)$ is computed as the zonally integrated cumulative meridional volume transport from the ocean bottom to depth z:

$$\Psi(z) = -\int_{z}^{-H} \int_{x_w}^{x_e} v(x, z')\, \mathrm{d}x\, \mathrm{d}z', \tag{4}$$

where v is the meridional velocity, and x_w and x_e denote the western and eastern boundaries of the basin. The negative sign accounts for the convention that northward transport is positive and ensures consistency with the standard definition of the overturning streamfunction.The AMOC strength is defined as the maximum value of $\Psi(z)$ over depth:

$$\text{AMOC} = \max_{z} \Psi(z), \tag{5}$$

This definition follows standard practices in both observational and modeling studies of the AMOC (Cunningham et al., 2007; McCarthy et al., 2015; Smeed et al., 2018).

3.5 Definition of Western Boundary Current (WBC) at 26.5°N

Analysis of data from the RAPID–MOCHA arrayat 26.5°N and construction of the AMOC timeseries uses transport estimates from the Florida Straits, the Antilles Current, and the interior ocean. In observations, the Florida Straits component represents a narrow and intense northward jet occurring between Bahamas and Florida that dominates the western boundary transport. However, The coarse horizontal resolution of CMIP6 models (1° x 1°) has bathymetry that is too coarse to represent the Bahamas, so there is no Florida Straits in the models.

Accordingly, the WBC region defined here should be interpreted as a model-resolved proxy that aggregates the western boundary contributions represented by the Florida Straits and the Antilles Current in RAPID observations. While this broader definition does not isolate the Florida Straits transport explicitly, it captures the dominant northward boundary flow that controls the western boundary contribution to meridional volume and C_{anth} transport in coarse-resolution climate models. This approach ensures consistency across models while maintaining physical comparability with the RAPID observational framework.

We define the WBC region based on the time-mean, depth-integrated meridional volume transport across the RAPID section. Meridional velocity is vertically integrated from the surface to the seafloor to obtain the column-integrated northward transport as a function of longitude, and then averaged over the 2004-2012 period. Longitudes where the resulting depth-integrated transport is positive are classified as the WBC domain (Fig. 5b), corresponding to approximately 80°W-70°W. Therefore, we define the WBC and non-WBC regions, where the non-WBC region represents the ocean interior outside the WBC.

3.6 Decomposition of C_{anth} Transport

To diagnose the parameters that govern projected future temporal variations in the meridional C_{anth} transport, we evaluate the time-dependent changes in both meridional velocity and carbon concentration relative to a reference state ($t = 0$, mark as t_0). Temporal anomalies are defined as

$$\Delta v(t) = v(t) - v(t_0), \qquad \Delta C(t) = C(t) - C(t_0).$$

Here, C represents C_{anth}. The corresponding change in total transport (ΔT) can then be written as

$$\Delta T(t) = \Delta(vC) = v(t_0)\,\Delta C(t) + C(t_0)\,\Delta v(t) + \Delta v(t)\,\Delta C(t), \tag{6}$$

where $v(t_0)$ and $C(t_0)$ denote the reference-state velocity and anthropogenic carbon concentration at January 2015, the beginning of the CMIP6 projection timeframe. The three terms on the right-hand side represent, respectively, the concentration-driven component $v(t_0)\,\Delta C(t)$, the velocity-driven component $C(t_0)\,\Delta v(t)$, and the nonlinear interaction term $\Delta v(t)\,\Delta C(t)$.

For spatial diagnosis, ΔT is integrated over distinct dynamic regions of the section: (1) the western boundary current (WBC, 80°W - 70°W), (2) the Non-WBC upper ocean (0–700 m, 70°W-10°W), and (3) the Non-WBC deep ocean (700 m - bottom, 70°W-10°W).

$$T_{\text{region}} = \iint_{\text{region}} \left[v(t_0)\,\Delta C(t) + C(t_0)\,\Delta v(t) + \Delta v(t)\,\Delta C(t)\right] dx\,dz. \tag{7}$$

This framework separates the effects of changes in velocity and concentration on total transport and allows quantification of their relative roles in driving the long-term evolution of T_{total}.

3.7 Time of emergence

To quantify when anthropogenic changes in C_{anth} transport become distinguishable from internal variability, we compute the Time of Emergence (ToE) for each SSP scenario using a trend-based signal-to-noise framework. The method follows established detectability approaches in which the externally forced response is represented by the ensemble-mean trend, and internal variability is quantified by the inter-member spread of trends (Schlunegger et al., 2019; McKinley et al., 2016; Hawkins & Sutton, 2012, 2009; Deser et al., 2012, 2020; Tebaldi & Friedlingstein, 2013).

To ensure consistency between the historical (2004-2014) and SSP (2015-2100) periods, we restrict the analysis to experiments that provide both tracer and velocity output across the two periods. After matching data availability, 7, 14, and 7 ensemble members are retained for SSP1-2.6, SSP2-4.5, and SSP5-8.5, respectively (Supplementary Table 1). For each selected experiment, the corresponding historical simulation over 2004-2014 is paired with its SSP continuation, and the two segments are concatenated to construct continuous time series spanning 2004-2100. All diagnostics, including C_{anth} transport, AMOC strength, and net volume transport, are expressed as annual means. They are computed from monthly data (see Section 3.2) and subsequently averaged over year, thereby reducing the influence of seasonal variability that can obscure long-term trends.

To estimate ToE, we apply an expanding time-window approach beginning in 2004. The terminal year y is progressively extended in five-year increments with a start from 5-year period (e.g., 2004–2009, 2004–2014, 2004–2019, ... 2004-2099). Within each window, linear trends are computed for each ensemble member.The externally forced signal is defined as the ensemble-mean trend across all members within a given window, thereby isolating the response to external forcing. Internal variability is quantified as the inter-member standard deviation of individual member trends relative to this ensemble mean (i.e., deviations of each member trend from the forced signal) within the same window. The signal-to-noise ratio (SNR) is then defined as the absolute value of the ensemble-mean trend divided by the inter-member standard deviation of trends. The ToE is identified as the earliest terminal year for which SNR ≥ 2, corresponding approximately to a 95% confidence threshold under Gaussian assumptions (McKinley et al., 2016, 2017). This definition evaluates the detectability of a forced trend in C_{anth} transport relative to internal variability in trend space, rather than instantaneous transport variability. The identified ToE therefore represents the minimum

observational record length required for the externally forced transport trend to become statistically distinguishable from background internal variability.

4 Results

4.1 Observed vs Simulated C_{anth} Transport

The CMIP6 ensemble well reproduces both the magnitude and variability of C_{anth} transport across the RAPID section (Fig. 1). All 55 simulations consistently indicate that the overturning circulation dominates total C_{anth} transport during 2004–2012 (Fig. 1a). The ensemble-mean transport over this period is 0.18 ± 0.02 PgC yr^{-1} (mean $\pm$ uncertainty in the ensemble time-series mean), in close agreement with the observational estimate of 0.19 ± 0.03 PgC yr^{-1} (Fig. 1b). Consistent with observations, the total transport is primarily driven by the northward overturning component (0.30 ± 0.02 PgC yr^{-1}), which accounts for approximately 71% of the total flux. This northward transport is partially offset by a southward horizontal component (-0.12 ± 0.00 PgC yr^{-1}), yielding a net northward C_{anth} transport across the section (Fig. 1b). The uncertainty here is calculated by the uncertainty among members and along the annual variability.

Beyond the mean state, CMIP6 simulations also capture the observed seasonal cycle of C_{anth} transport (Fig. 2). The models reproduce both the phase and overall structure of the seasonal variability, with a maximum in July–August and a minimum in March–April. Throughout the year, variability in total C_{anth} transport is largely governed by changes in the overturning component (Fig. 2a,c–d), consistent with observational analyses. The simulated seasonal amplitude range from 0.15 ± 0.04 PgC yr^{-1} to 0.23 ± 0.05 PgC yr^{-1} , somewhat smaller than the observed amplitude of 0.23 ± 0.05 PgC yr^{-1} to 0.25 ± 0.05 PgC yr^{-1} (Fig. 2a). This difference may be due to disparities in temporal sampling. RAPID observations are based on 10-day estimates that are subsequently averaged to monthly means, whereas model outputs represent averages over high-frequency internal time steps prior to archiving. As a result, modeled monthly means may appear smoother than the observational estimates.

Despite the overall agreement with observations in both mean state and seasonal phase, differences in the seasonal cycle across the CMIP6 ensemble primarily reflect structural discrepancies between models rather than internal variability within individual ensembles (Fig. 2b–d). Variability among ensemble members of a given model is relatively small, indicating that internal variability plays a secondary role in shaping the seasonal amplitude and structure. Instead, the dominant source of spread arises from inter-model differences, particularly between CanESM and CESM2. The CanESM ensemble mean is quantitatively closer to RAPID observations, both in terms of seasonal amplitude and the timing of extrema (Fig. 2b). The two models also exhibit distinct seasonal structures: CanESM shows two peaks of comparable magnitude in summer and winter, whereas CESM2 displays a pronounced summer maximum that substantially exceeds its winter peak. These structural differences are primarily associated with the overturning component (Fig. 2c–d), which, as noted above, governs most of the seasonal variability in total C_{anth} transport.

4.2 Future changes of C_{anth} transport in RAPID

The agreement between CMIP6 simulations and observations provides confidence in using model projections to assess changes in C_{anth} transport at the RAPID section. Prior to the emergence of observationally constrained anthropogenic carbon transport in the late 1950s, northward C_{anth} transport at 26.5°N increased only slowly, with a nearly negligible trend (Fig. 3a). This weak increase likely reflects the early stage of industrialization, when atmospheric CO_2 concentrations and oceanic anthropogenic carbon uptake were still relatively low. From the mid-20th century onward (1950-2000), C_{anth} transport began to rise more rapidly, with a trend of approximately 0.02 PgC yr^{-1} decade^{-1}. The timing of

this is consistent with the acceleration of anthropogenic emissions and the corresponding intensification of ocean carbon uptake.

Entering the 21st century, C_{anth} transport continues to increase under all scenarios, but the rate of increase diverges across emission pathways. During 2000-2050, the trend strengthens to 0.04 PgC yr^{-1} $decade^{-1}$ under low-emission (SSP1-2.6), 0.05 PgC yr^{-1} $decade^{-1}$ under intermediate-emission (SSP2-4.5), and 0.06 PgC yr^{-1} $decade^{-1}$ under high-emission (SSP5-8.5). After mid-century, this scenario dependence becomes increasingly pronounced. Under SSP5-8.5, the rapid increase persists throughout 2050-2100, with a growth rate comparable to that in the first half of the century. In contrast, the trend under SSP2-4.5 weakens to approximately 0.02 PgC yr^{-1} $decade^{-1}$, similar to late 20th-century levels, while under SSP1-2.6 it declines further and approaches stabilization. Superimposed on these long-term changes, interannual variability also increases toward the end of the century (Fig. 3a).

Beyond interannual variability, the seasonal variability of C_{anth} transport also intensifies under future warming, in addition to the long-term mean increase (Fig. S2a). To quantify this change, we compare the climatological seasonal cycles between the early and late 21st century across SSP scenarios. During the early period (Fig. S2b), the seasonal cycles are broadly similar across scenarios, with only modest differences in both mean state and amplitude. In contrast, by the late century (Fig. S2c), a clear separation emerges: while the phase remains largely unchanged, both the mean transport and the amplitude of seasonal variability increase substantially. The strongest amplification occurs under SSP5–8.5, with the mean increasing by 81% and the variability by 35%.

The increase in C_{anth} transport is consistent with changes in C_{anth} concentration, which in turn closely follow atmospheric CO_2 trajectories (Fig. 3b). The area-weighted mean oceanic C_{anth} concentration at the RAPID section increases and accelerates over time. During 2000–2050, the growth rates are 0.18 mmol m^{-3} yr^{-1} under SSP1–2.6, 0.20 mmol m^{-3} yr^{-1} under SSP2–4.5, and 0.21 mmol m^{-3} yr^{-1} under SSP5–8.5.After mid-century, the divergence among scenarios becomes more pronounced. Under SSP5–8.5, the growth rate further accelerates to approximately 1.7 times the early-century rate. In contrast, SSP2–4.5 remains relatively stable, whereas SSP1–2.6 shows a marked decline, with growth rates reduced to about 60% of their earlier values.

On the contrary, the increase in C_{anth} transport occurs alongside a systematic weakening of the overturning circulation. Across all SSP scenarios, both AMOC strength and net volume transport decline under continued warming (Fig. 3c–d). We retain the net volume transport here because it provides a transport-based quantity that is more directly comparable to C_{anth} transport than AMOC strength alone. While AMOC strength characterizes the large-scale overturning circulation, C_{anth} transport depends directly on the product of carbon concentration and the velocity field. The decline in net volume transport therefore provides useful context for interpreting why the increase in C_{anth} transport cannot be attributed to an increase in circulation strength. During 2004–2050, the net volume transport decreases at rates of -0.27 ± 0.14 Sv $decade^{-1}$ (SSP1-2.6), -0.24 ± 0.15 Sv $decade^{-1}$ (SSP2-4.5), and -0.33 ± 0.10 Sv $decade^{-1}$ (SSP5-8.5). This weakening persists into the late century (2050–2100), with trends of -0.18 ± 0.05 Sv $decade^{-1}$, -0.39 ± 0.09 Sv $decade^{-1}$, and -0.54 ± 0.06 Sv $decade^{-1}$, respectively (Fig. 3c). A comparable decline is observed in AMOC strength (Fig. 3d), indicating a robust weakening of the overturning circulation across all emission scenarios.

Thus, the continued strengthening of northward C_{anth} transport occurs despite a concurrent weakening of overturning circulation. This divergence between declining volume transport and increasing C_{anth} concentration is essential for understanding the mechanisms governing future anthropogenic carbon redistribution at the RAPID section.

4.3 Structure of C_{anth} transport

Because the increase in C_{anth} transport cannot be explained by changes in section-integrated circulation strength alone, we next examine how carbon transport is distributed across the RAPID section. The apparent decoupling between AMOC weakening and increasing C_{anth} transport arises from strongly non-uniform spatial contributions across the RAPID section (Fig. 4). C_{anth} transport is largest in the upper 0–700 m of the WBC, collocated with the most intense northward flow (Fig. 4a,b). This spatial structure persists under future emission scenarios, but with amplified magnitudes (Fig. 4d and g; Fig. S4d and g). Outside the WBC, C_{anth} transport is predominantly southward, particularly in the upper 0–700 m, where southward currents coincide with enhanced C_{anth} concentrations (Fig. 4i; Fig. S4i). Overall, the interior southward export compensates for approximately two-thirds of the northward C_{anth} transport within the WBC (64–68% throughout the period; Fig. 5a). This zonal compensation between the WBC and the basin interior represents a robust and persistent structural feature of the RAPID section (Fig. 4).

Vertical integration further highlights that the WBC absolute magnitude changes substantially across all emission scenarios, even though the percentage of the total does not. The C_{anth} transport in WBC is 0.88 PgC yr^{-1} under SSP1–2.6, 1.02 PgC yr^{-1} under SSP2–4.5, and 1.22 PgC yr^{-1} under SSP5–8.5 (Fig. 5a). In contrast, the WBC volume transport weakens more substantially under higher-emission scenarios, decreasing from 22 Sv during 2004–2012 to 19.8 Sv under SSP1–2.6 and 17.8 Sv under SSP5–8.5 (Fig. 5b). Despite this weakening, the fractional contribution of the WBC to total RAPID C_{anth} transport remains approximately 54% across all scenarios. In contrast to the transport response, the column-integrated C_{anth} exhibits an opposite spatial pattern: the interior basin shows substantially higher concentrations than the WBC region where with higher current speed (Fig. 5c).

To further elucidate the vertical structure of C_{anth} transport, we examine depth-integrated transports across the RAPID section (Fig. 5d,e). For each longitude, C_{anth} transport and volume transport are first vertically integrated from the surface to a given depth, yielding cumulative water-column transports, which are then integrated zonally to obtain the total RAPID-section transport as a function of depth. Both C_{anth} transport and volume transport increase rapidly from the surface to approximately 700 m, indicating that the upper ocean dominates the northward export (Fig. 5d,e). Below 700 m, the cumulative northward transport weakens with depth, reflecting increasing southward contributions from deeper layers. The zonal-mean C_{anth} concentration exhibits a markedly different vertical structure: elevated concentrations are confined primarily to the upper 700 m, where the separation among emission scenarios is most pronounced (Fig. 5f). Across all depths, C_{anth} concentrations are largest under SSP5–8.5, followed by SSP2–4.5 and SSP1–2.6, and are smallest during the historical period. The weak but nonzero C_{anth} signal below 700 m may reflect deeper ventilation and storage pathways, particularly those associated with subpolar North Atlantic water-mass formation, although a full diagnosis of these processes is beyond the scope of this study.

4.4 Physical drivers of C_{anth} transport change

To quantify the contributions to total C_{anth} transport, we partition the RAPID section into three regions (Fig. 6a): (1) the western boundary current (WBC), (2) the upper interior (Non-WBC, 0-700 m), and (3) the deep interior (Non-WBC, 700 m to bottom). The northward C_{anth} transport is primarily driven by the WBC, which exhibits a persistent increase from 2015 to 2100 and dominates the net enhancement of total transport. In contrast, the interior ocean is characterized by southward transport, with the upper interior showing a strengthening export that partially offsets the WBC contribution. In magnitude, the WBC transport is approximately 1.6-1.7 times larger than the opposing transport in the interior, highlighting its dominant role in setting the net northward flux. The deep interior contributes negligibly, accounting for only about 2-5% of the total interior transport, and

shows little change over the century. These results indicate a strong spatial asymmetry in C_{anth} transport, with boundary currents controlling the net flux while interior pathways act primarily as a compensating return flow.

To isolate the underlying physical drivers, we decompose the total change in C_{anth} transport, $\Delta(CV)$, into three components (Eq. 6): $V(t_0)\Delta C(t)$, representing the effect of increasing C_{anth} concentration under fixed velocity; $C(t_0)\Delta V(t)$, representing velocity changes under fixed concentration; and $\Delta V(t)\Delta C(t)$, the nonlinear interaction term. In Fig. 6b, $V(t_0)\Delta C(t)$ term exhibits a sustained and dominant positive trend throughout the century, increasing steadily to approximately 0.5 PgC yr^{-1} by 2100. In contrast, both the $C(t_0)\Delta V(t)$ and $\Delta V(t)\Delta C(t)$ terms remain persistently negative, with magnitudes of about -0.15 and -0.1 PgC yr^{-1}, respectively. These opposing contributions indicate that while changes in circulation act to weaken the northward transport, they are outweighed by the effect of increasing C_{anth} concentration.

Importantly, the roles of concentration and circulation differ across timescales. The long-term increase in total C_{anth} transport is primarily controlled by the accumulation of C_{anth}. In contrast, variability in the velocity field plays a key role in shaping the temporal fluctuations of transport, including the seasonal cycle and its increasing amplitude. Regionally, the dominant role of the $V_0\Delta C$ term is evident in both the WBC and the upper interior, albeit with opposite signs (Fig. 6c-d). This mechanism hierarchy is same under low-emission and high-emission scenario (Fig. S6, Fig. S7). Across all scenarios, rising upper-ocean C_{anth} concentration emerges as the primary driver of future transport intensification, particularly within the WBC. As the primary northward upper branch of the AMOC at the RAPID section, the WBC continues to efficiently export elevated upper-ocean C_{anth} signals under future warming despite AMOC weakening, indicating that concentration increases increasingly outweigh the effects of reduced circulation strength.

Together, these results demonstrate that future changes in C_{anth} transport arise from a concentration-driven intensification of the mean state, modulated by circulation-driven variability. This is consistent with Brown et al. (2021), which highlighted the importance of C_{anth} concentration in controlling transport variability, and further extends it by showing that concentration changes increasingly dominate the long-term trend under future warming.

4.5 Time of emergence and detectability of C_{anth} transport trends

On centennial timescales, C_{anth} transport is expected to increase in response to the sustained rise in oceanic anthropogenic carbon inventories (Sabine et al., 2004; Gruber et al., 2019; Müller et al., 2023). However, over short observational periods, internally driven ocean variability can strongly modulate interannual-to-decadal fluctuations in transport and may obscure, or even temporarily reverse, the apparent forced trend. For example, RAPID-based estimates over 2004–2012 report no trend in C_{anth} transport (Brown et al., 2021), in contrast to the long-term increase. This discrepancy highlights the difficulty of detecting forced signals in the presence of substantial internal variability.

To quantify detectability, we define the ToE as the first year when the forced signal exceeds twice the standard deviation of internal variability (McKinley et al., 2016; Schlunegger et al., 2020). Across all scenarios, C_{anth} transport exhibits relatively early emergence, on the order of two to three decades (Fig. 7a). Specifically, ToE occurs in 2033 under SSP1-2.6, 2028 under SSP2-4.5, and 2023 under SSP5-8.5, indicating that stronger forcing leads to earlier detectability through an enhanced signal-to-noise ratio.

In comparison, circulation-based metrics exhibit substantially delayed emergence. AMOC strength emerges in 2042 under SSP1-2.6, 2038 under SSP2-4.5, and 2033 under SSP5-8.5, approximately a decade later than C_{anth} transport (Fig. 7b). Net volume transport emerges even later, with ToE occurring in 2078 under SSP1-2.6, 2063 under SSP2-4.5, and 2053 under SSP5-8.5 (Fig. 7c), corresponding to delays of about 25–45 years relative to C_{anth} transport.

These differences in emergence time may arise from distinct signal-to-noise structures in carbon and circulation fields. As shown in Section 4.4, C_{anth} transport is primarily controlled by upper-ocean C_{anth} concentration, whose changes closely follow external atmospheric CO_2 forcing. Because these concentration increases are spatially coherent and largely confined to the upper ocean, they amplify the forced signal relative to internal variability, enabling earlier detectability. By comparison, volume transport depends on both circulation variability and deep-ocean adjustment, which involve slower dynamical processes and larger intrinsic variability, thereby delaying its emergence.

5 Discussion and Conclusions

The CMIP6 ensemble reproduces both the mean magnitude and seasonal cycle of C_{anth} transport across 26.5°N in close agreement with RAPID observations (Brown et al., 2021), providing confidence in the model-based projections. Across all scenarios, C_{anth} transport continues to increase beyond the point at which AMOC magnitude begins to decline. This apparent divergence reflects a compensation between circulation and concentration effects: rising upper-ocean C_{anth} concentrations increasingly outweigh reductions in northward flow, resulting in a net enhancement of C_{anth} flux. By extending observational partitioning approaches (Brown et al., 2021) into the future, we demonstrate that long-term changes in C_{anth} transport are progressively dominated by concentration-driven mechanisms rather than by overturning variability (Fig.1a).

The spatial structure of this response is set primarily by the upper ocean and WBC. Scenario-dependent increases in C_{anth} are concentrated within the upper 700 m, where ocean carbon responds most directly to atmospheric CO_2 forcing. Strong northward velocities within the WBC efficiently export this amplified surface signal, allowing concentration increases to dominate over modest reductions in transport volume (Fig.6). Enhanced southward flow in the basin interior partially compensates this signal but does not offset it. These results are consistent with studies emphasizing western boundary advection as a key regulator of anthropogenic carbon redistribution and downstream subpolar uptake (Ridge & McKinley, 2020; Nickford et al., 2022).

A key result of this study is the estimated hierarchy in the time of emergence among different RAPID-based diagnostics, which has direct implications for observational detectability. The relatively early emergence of C_{anth} transport arises from its strong dependence on C_{anth} concentration changes, which respond rapidly to atmospheric CO_2 forcing through air–sea exchange. As a result, the current RAPID observational record (2004–2025), spanning approximately two decades, is already approaching the emergence timescale of C_{anth} transport, particularly under intermediate-emission scenarios. In contrast, circulation-based metrics such as AMOC strength and net volume transport reflect slower dynamical adjustments and larger intrinsic variability, which delay their detectability. Detecting a robust trend in AMOC strength will likely require at least two additional decades of sustained observations, whereas full-depth volume transport may not emerge for another three to five decades. These results suggest that anthropogenic carbon transport may provide an earlier and more robust observational indicator of climate-driven ocean change than circulation-based metrics. Moreover, continued observations at the RAPID array remain necessary, as detecting robust changes in AMOC and large-scale circulation will likely require at least one to three additional decades of sustained measurements.

Several sources of uncertainty should be noted. The ToE estimates are derived from a single-model large ensemble (CanESM), which may underestimate structural uncertainty across models. In addition, CanESM exhibits relatively weak AMOC variability compared to other models such as CESM (Weijer, Cheng, et al., 2020), potentially leading to earlier simulated emergence. These factors suggest that the actual emergence of circulation signals may occur later than estimated here, further highlighting the value of sustained observations at the RAPID section for resolving the ocean response to climate change. In addition, part

of the apparent divergence between AMOC weakening and increasing C_{anth} transport may reflect the section-based nature of the RAPID diagnostics. The RAPID array captures transports across 26.5°N rather than the full basin-scale Atlantic overturning circulation, and local compensation between the WBC and basin interior may make the relationship between AMOC variability and C_{anth} transport harder to identify at this section. Thus, the inferred AMOC–C_{anth} relationship should be interpreted as a RAPID-section perspective rather than a complete constraint on the basin-scale overturning-carbon transport balance.

Taken together, our results highlight a fundamental distinction between carbon-cycle and circulation responses in the North Atlantic. While anthropogenic carbon signals respond rapidly to atmospheric forcing and become detectable on decadal timescales, circulation changes emerge more slowly due to their dynamical complexity and intrinsic variability. Continued operation of the RAPID observational program will therefore provide important constraints on both the early evolution of carbon transport and the longer-term adjustment of ocean circulation under sustained anthropogenic forcing.

Acknowledgments

This project is supported by the US National Science Foundation (Awards OCE2400433 and AGS2019625). We acknowledge the World Climate Research Programme's Working Group on Coupled Modelling (WGCM), which is responsible for CMIP, and thank the climate modeling groups for producing and making their model output available. We also acknowledge the ROCCA project for providing the observational estimates of anthropogenic carbon (C_{anth}) used in this study. The data used in this analysis are publicly available from the Earth System Grid Federation (ESGF) CMIP6 archive (https://esgf-node.llnl.gov/search/cmip6/) and the ROCCA observational dataset repository.

This work was also supported by UK Natural Environment Research Council grants UKRI-NERC NE/W009560/1 (C-Streams), UKRI-NERC NE/Y005287/1 (ROCCA), and UKRI-NERC NE/Y005589/1 (Atlantis). In addition, we acknowledge support from the European Union under grant agreement no. 101059547 (EPOC) and no. 101083922 (Ocean-ICU), and from UK Research and Innovation (UKRI) under the UK government's Horizon Europe funding guarantee [grant numbers 10054454, 10063673, 10064020, 10059241, 10079684, 10059012, and 10048179]. Views and opinions expressed are, however, those of the authors only and do not necessarily reflect those of the European Union or the European Research Executive Agency. Neither the European Union nor the granting authority can be held responsible for them.

References

Brown, P. J., et al. (2021). Observed transport of anthropogenic carbon at 26.5°n in the atlantic ocean. *Global Biogeochemical Cycles*, *35*(3), e2020GB006879. doi: 10.1029/2020GB006879

Cunningham, S. A., et al. (2007). Temporal variability of the atlantic meridional overturning circulation at 26.5°n. *Science*, *317*, 935–938. doi: 10.1126/science.1141304

Danabasoglu, G., Lamarque, J.-F., Bacmeister, J., Bailey, D. A., DuVivier, A. K., Edwards, J., ... (2020). The community earth system model version 2 (cesm2). *Journal of Advances in Modeling Earth Systems*, *12*(2), e2019MS001916. doi: 10.1029/2019MS001916

Deser, C., Lehner, F., Rodgers, K. B., Ault, T., Delworth, T. L., et al. (2020). Insights from earth system model initial-condition large ensembles and future prospects. *Nature Climate Change*, *10*, 277–286. doi: 10.1038/s41558-020-0731-2

Deser, C., Phillips, A. S., Bourdette, V., & Teng, H. (2012). Uncertainty in climate change projections: The role of internal variability. *Climate Dynamics*, *38*, 527–546. doi: 10.1007/s00382-010-0977-x

DeVries, T. (2014). The oceanic anthropogenic co_2 sink: storage, air–sea fluxes, and transports over the industrial era. *Global Biogeochemical Cycles*, *28*, 631–647. doi: 10.1002/2013GB004739

Friedlingstein, P., O'Sullivan, M., Jones, M. W., Andrew, R. M., Bakker, D. C. E., Hauck, J., ... Zeng, J. (2025). Global carbon budget 2025. *Earth System Science Data Discussions*. doi: 10.5194/essd-2025-659

Goris, N., Tjiputra, J., Olsen, A., Schwinger, J., Lauvset, S. K., & Jeansson, E. (2018). Constraining projection-based estimates of the future north atlantic carbon uptake. *Journal of Climate*, *31*(10), 3959–3978. doi: 10.1175/JCLI-D-17-0564.1

Gruber, N., Gloor, M., Fletcher, S. E. M., Doney, S. C., Dutkiewicz, S., Follows, M. J., ... Takahashi, T. (2009). Oceanic sources, sinks, and transport of atmospheric co_2. *Global Biogeochemical Cycles*, *23*(1), GB1005. doi: 10.1029/2008GB003349

Gruber, N., et al. (2019). The oceanic sink for anthropogenic co_2 from 1994 to 2007. *Science*, *363*, 1193–1199. doi: 10.1126/science.aau5153

Gruber, N., Sarmiento, J. L., & Stocker, T. F. (1996). An improved method for detecting anthropogenic co in the oceans. *Global Biogeochemical Cycles*, *10*(4), 809-837. doi: 10.1029/96GB01608

Hawkins, E., & Sutton, R. (2009). The potential to narrow uncertainty in regional climate predictions. *Bulletin of the American Meteorological Society*, *90*(8), 1095–1108. doi: 10.1175/2009BAMS2607.1

Hawkins, E., & Sutton, R. (2012). Time of emergence of climate signals. *Geophysical Research Letters*, *39*(1), L01702. doi: 10.1029/2011GL050087

IPCC. (2021). *Climate change 2021: The physical science basis. contribution of working group i to the sixth assessment report*. Cambridge University Press.

IPCC. (2023). *Climate change 2023: Synthesis report. contribution of working groups i, ii and iii to the sixth assessment report of the intergovernmental panel on climate change.* Geneva, Switzerland. doi: 10.59327/IPCC/AR6-9789291691647

Khatiwala, S., et al. (2013). Global ocean storage of anthropogenic carbon. *Biogeosciences*, *10*, 2169–2191. doi: 10.5194/bg-10-2169-2013

Khatiwala, S., Primeau, F., & Hall, T. (2009). Reconstruction of the history of anthropogenic co_2 concentrations in the ocean. *Nature*, *462*, 346–349. doi: 10.1038/nature08526

Lauvset, S. K., et al. (2023). Glodapv2.2023: an update of the global interior ocean biogeochemical data product. *Earth System Science Data*.

Macdonald, A. M., Baringer, M. O., Wanninkhof, R., Lee, K., & Wallace, D. W. R. (2003). A 1998–1992 comparison of inorganic carbon and its transport across 24.5° n in the atlantic. *Deep-Sea Research Part II: Topical Studies in Oceanography*, *50*, 3041–3064. doi: 10.1016/S0967-0645(03)00137-3

McCarthy, G. D., Hug, G., Smeed, D., Morris, K. J., & Moat, B. (2025). Signal and noise

in the atlantic meridional overturning circulation at 26°n. *Geophysical Research Letters*, *52*(7), e2025GL115055. doi: 10.1029/2025GL115055

McCarthy, G. D., Smeed, D. A., Johns, W. E., Frajka-Williams, E., Moat, B. I., Rayner, D., ... Bryden, H. L. (2015). Measuring the atlantic meridional overturning circulation at 26°n. *Progress in Oceanography*, *130*, 91–111. doi: 10.1016/j.pocean.2014.10.006

McKinley, G. A., Fay, A. R., Eddebbar, Y. A., Gloege, L., & Lovenduski, N. S. (2020). External forcing explains recent decadal variability of the ocean carbon sink. *AGU Advances*, *1*(2), e2019AV000149. doi: 10.1029/2019AV000149

McKinley, G. A., Fay, A. R., & Lovenduski, N. S. (2017). Convergent evidence for marine carbon cycle feedbacks. *Science*, *358*(6368), 1197–1201. doi: 10.1126/science.aao2959

McKinley, G. A., Pilcher, D. J., Fay, A. R., Lindsay, K., Long, M. C., & Lovenduski, N. S. (2016). Timescales for detection of trends in the ocean carbon sink. *Nature*, *530*, 469–472. doi: 10.1038/nature16958

Moat, B. I., Smeed, D. A., Rayner, D., Johns, W. E., Smith, R., Volkov, D., ... Collins, J. (2026). *Atlantic meridional overturning circulation observed by the rapid-mocha-wbts (rapid-meridional overturning circulation and heatflux array-western boundary time series) array at 26n from 2004 to 2024 (v2024.1a).* British Oceanographic Data Centre - Natural Environment Research Council, UK. doi: 10.5285/48d0bf43-0598-ceb2-e063-7086abc062f1

Müller, J. D., Gruber, N., Carter, B., Feely, R., Ishii, M., Lange, N., & et al. (2023). Decadal trends in the oceanic storage of anthropogenic carbon from 1994 to 2014. *AGU Advances*, *4*(4). doi: 10.1029/2023AV000875

Nickford, S., Palter, J. B., Donohue, K. A., Fassbender, A. J., Gray, A. R., Long, J., ... Takeshita, Y. (2022). Autonomous wintertime observations of air-sea exchange in the Gulf Stream reveal a perfect storm for ocean CO2 uptake. *Geophysical Research Letters*, *49*(5). doi: 10.1029/2021GL096805

Ridge, S. M., & McKinley, G. A. (2020). Advective controls on the North Atlantic anthropogenic carbon sink. *Global Biogeochemical Cycles*, *34*(7). doi: 10.1029/2019GB006457

Sabine, C. L., et al. (2004). The oceanic sink for anthropogenic co_2. *Science*, *305*, 367–371. doi: 10.1126/science.1097403

Schlunegger, S., Rodgers, K. B., Sarmiento, J. L., Frölicher, T. L., Dunne, J. P., Ishii, M., & Slater, R. (2019). Emergence of anthropogenic signals in the ocean carbon cycle. *Nature Climate Change*, *9*, 719–725. doi: 10.1038/s41558-019-0553-2

Schlunegger, S., Rodgers, K. B., Sarmiento, J. L., Ilyina, T., Dunne, J. P., Takano, Y., ... Lehner, F. (2020). Time of emergence and large ensemble intercomparison for ocean biogeochemical trends. *Global Biogeochemical Cycles*, *34*(8), e2019GB006453. doi: 10.1029/2019GB006453

Sigmond, M., Anstey, J., Arora, V., Digby, R., Gillett, N., Kharin, V., ... Yang, D. (2023). Improvements in the canadian earth system model (canesm) through systematic model analysis: Canesm5.0 and canesm5.1. *Geoscientific Model Development*, *16*(21), 6553–6596. doi: 10.5194/gmd-16-6553-2023

Smeed, D. A., et al. (2018). The north atlantic ocean is in a state of reduced overturning. *Geophysical Research Letters*, *45*, 1527–1533. doi: 10.1002/2017GL076350

Swart, N. C., Cole, J., Kharin, S., Lazare, M., Scinocca, J., Gillett, N. P., ... Winter, B. (2019a). *The canadian earth system model (canesm) – v5.0.3.* Zenodo [code]. doi: 10.5281/zenodo.3251114

Swart, N. C., Cole, J. N. S., Kharin, V. V., Lazare, M., Scinocca, J. F., Gillett, N. P., ... Winter, B. (2019b). The canadian earth system model version 5 (canesm5.0.3). *Geoscientific Model Development*, *12*, 4823–4873. doi: 10.5194/gmd-12-4823-2019

Tebaldi, C., & Friedlingstein, P. (2013). Delayed detection of climate mitigation benefits due to climate inertia and variability. *Proceedings of the National Academy of Sciences of the United States of America*, *110*(43), 17229–17234. doi: 10.1073/pnas.1300005110

Weijer, W., Cheng, W., Garuba, O. A., Hu, A., & Nadiga, B. T. (2020). Cmip6 models predict significant 21st century decline of the atlantic meridional overturning circulation.

Geophysical Research Letters, *47*(12), e2019GL086075. doi: 10.1029/2019GL086075

Weijer, W., Sijp, W. P., Watanabe, M., Karspeck, A., Hu, A., Cheng, W., ... Gille, S. T. (2020). Sensitivity of the atlantic meridional overturning circulation to climate change. *Geophysical Research Letters*, *47*(11), e2019GL086075. doi: 10.1029/2019GL086075

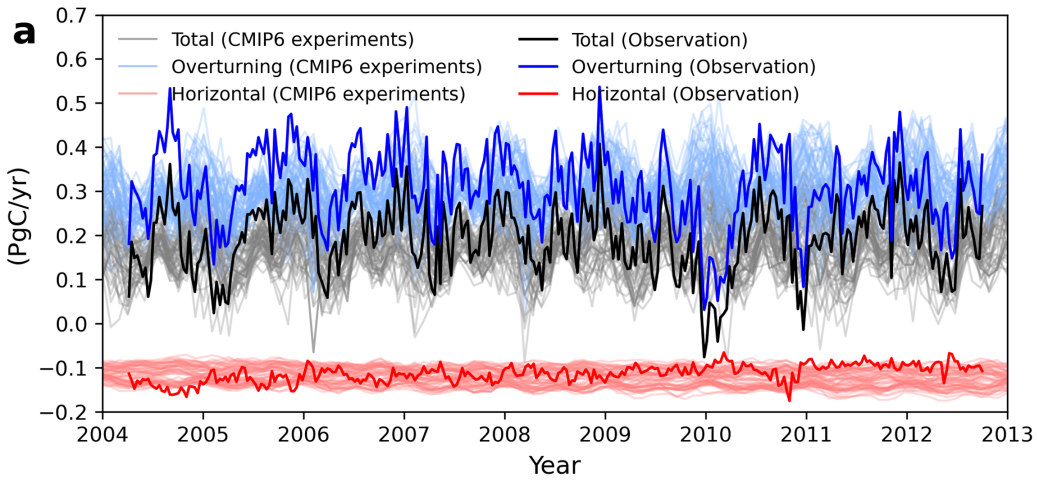

b

2004-2012	Observation	CMIP6
Total	+0.19 ± 0.03 PgC yr^{-1}	+0.18 ± 0.02 PgC yr^{-1}
Overturning	+0.31± 0.04 PgC yr^{-1}	+0.30 ± 0.02 PgC yr^{-1}
Horizontal	-0.11 ± 0.01 PgC yr^{-1}	−0.12 ± 0.00 PgC yr^{-1}

Figure 1. Observed vs. CMIP6 simulated anthropogenic carbon transport (C_{anth}) across the RAPID 26.5° N section. (a) Time series of total C_{anth} transport (black) and its components of overturning (blue) and horizontal (red) terms during 2004-2012. Thick lines denote observations, and light-colored lines show the individual results of 55 CMIP6 experiments during the same period (gray for total, light blue for overturning, and light red for horizontal). Positive values indicate northward transport, and negative values indicate southward transport. (b) Time-series mean (± 1 seasonal standard deviation) of the observed results and the ensemble mean of the 55 CMIP6 simulations during 2004-2012. For CMIP6, the shaded range represents the ensemble spread of the member-wise seasonal standard deviations: we first compute the seasonal standard deviation within each member, and then take the standard deviation across members.

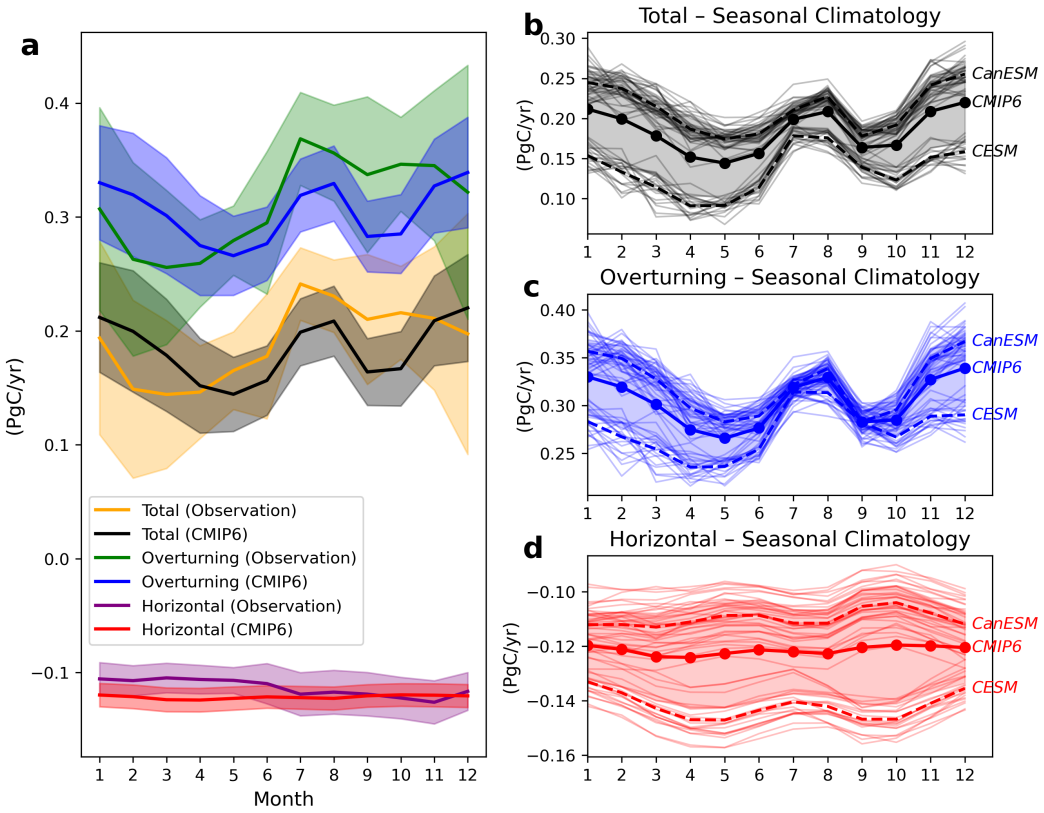

Figure 2. Seasonal cycle of C_{anth} transport across the RAPID 26.5° N section. (a) Monthly climatology of total (black), overturning (blue), and horizontal (red) components of C_{anth} transport for the period 2004-2012 in observations, with shading indicating one standard deviation of monthly variability. Positive values denote northward transport. Monthly climatology of total (orange), overturning (green), and horizontal (purple) components of C_{anth} transport of CMIP6 ensemble means. (b-d) Seasonal climatologies of total (b), overturning (c), and horizontal (d) C_{anth} transport from individual CMIP6 experiments. The gray, blue, and red shading respectively denote total, overturning, and horizontal components, consistent with panel (a) and representing one standard deviation. Black, blue, and red solid circles mark the CMIP6 ensemble mean seasonal cycle. Highlighted solid lines represent the ensemble means of CanESM and CESM, while lighter lines show individual results from the 55 CMIP6 experiments.

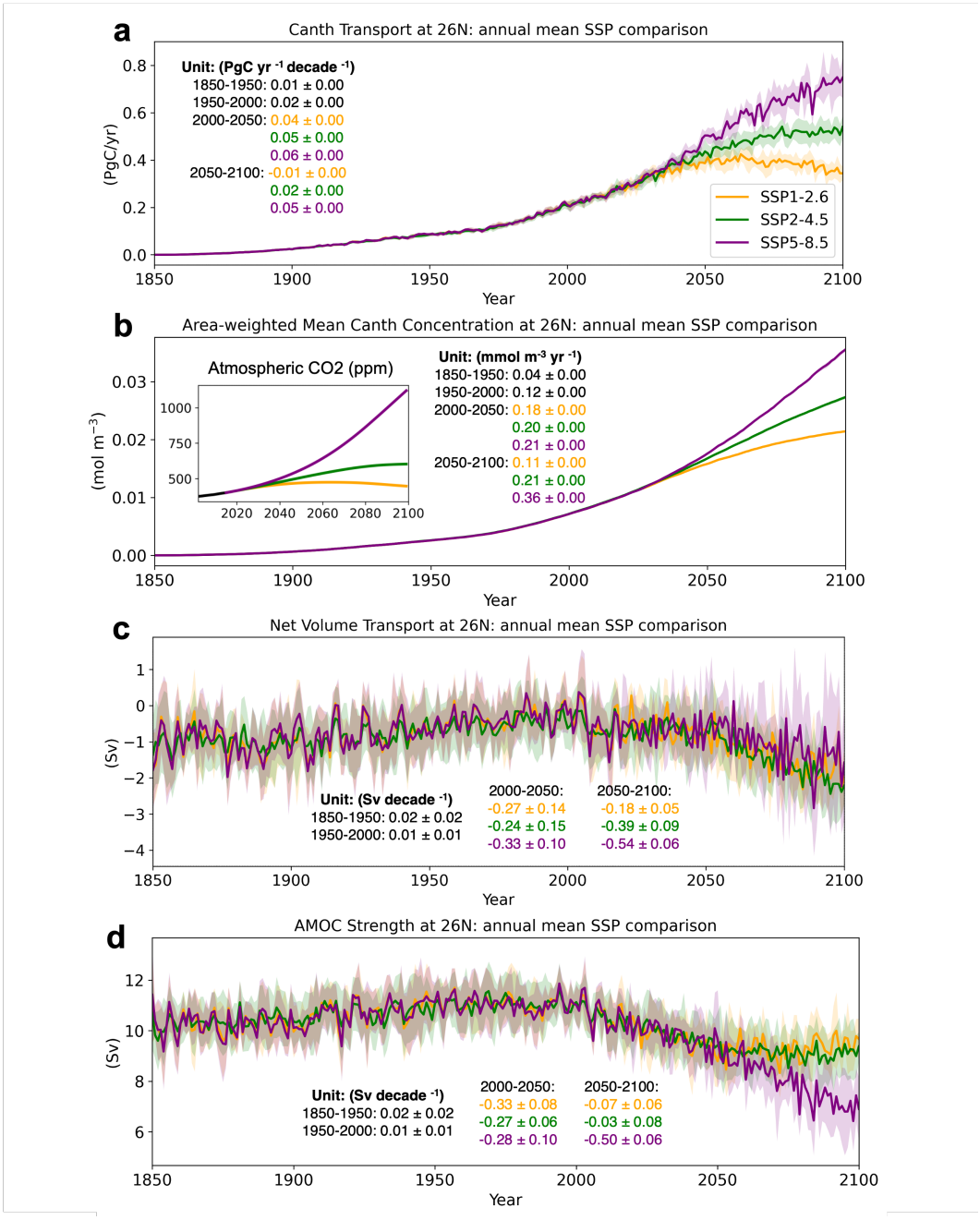

Figure 3. Evolution of C_{anth} transport and volume transport at the RAPID 26°N section based on CMIP6 dataset. (a) Time series of C_{anth} transport for the historical period (1850-2014) and three future scenarios (2015-2100): SSP1-2.6 (orange), SSP2-4.5 (green), and SSP5-8.5 (purple). Solid lines denote the ensemble mean and shaded regions indicate the inter-member spread (±1 standard deviation). The in-panel table summarizes linear trends for different periods (1850-1950, 1950-2000, 2004-2050, and 2050-2100), with text colors corresponding to each SSP curve. Uncertainties represent the inter-member spread of the trend estimates. Positive values indicate northward transport. (b) Area-weighted mean C_{anth} concentration at the RAPID section. The inset shows the corresponding atmospheric CO_2 trajectories under each SSP scenario, representing low- (SSP1-2.6, orange), intermediate- (SSP2-4.5, green), and high- (SSP5-8.5, purple) emission pathways. Trend values for each period are annotated as in panel (a). (c) Net volume transport across the RAPID section at 26°N. Positive values indicate northward transport. Lines and shading follow the same convention as in panel (a), and the in-panel table shows period-specific trends and their inter-member spread. (d) AMOC strength at 26°N. Solid lines denote the ensemble mean and shading represents the inter-member spread. The in-panel table shows phase-dependent trends and their spread across ensemble members. All trends are derived from linear regression over the specified periods. Details of the CMIP6 experiments used for each scenario are provided in Supplementary Table 1.

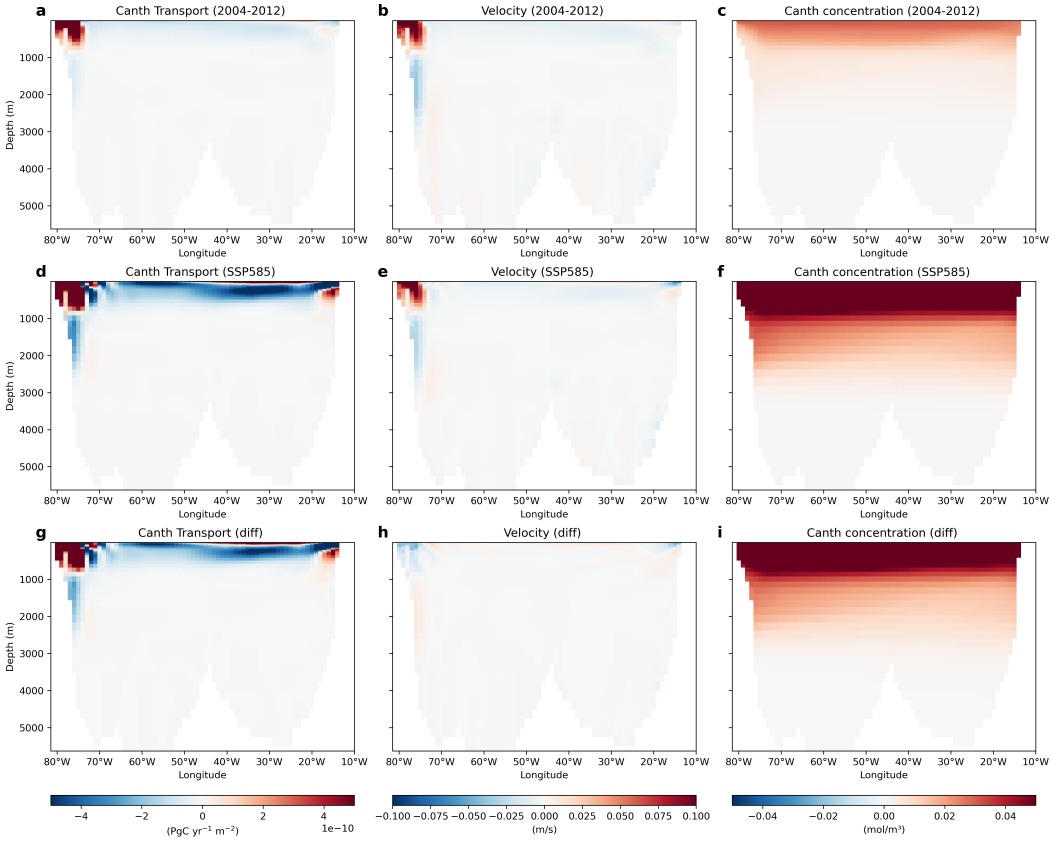

Figure 4. Spatial structure of C_{anth} transport and its drivers across the RAPID 26.5°N section under historical and future scenarios. (a-c) Time-mean zonal-vertical sections of C_{anth} transport, meridional velocity, and C_{anth} for the historical period (2004-2012). positive values (red) indicates northward C_{anth} transport. (d-f) Same as (a-c), but for the SSP5-8.5 scenario during 2015-2100. Results for SSP1-2.6 and SSP2-4.5 are shown in Fig. S4. (g-i) Differences between SSP5-8.5 (d-f) and the historical period (a-c), showing changes in C_{anth} transport, velocity, and C_{anth} concentration, respectively. Red shading (positive values) indicates an increase in SSP5-8.5 relative to the historical period. Results for SSP1-2.6 and SSP2-4.5 are shown in Fig. S4.

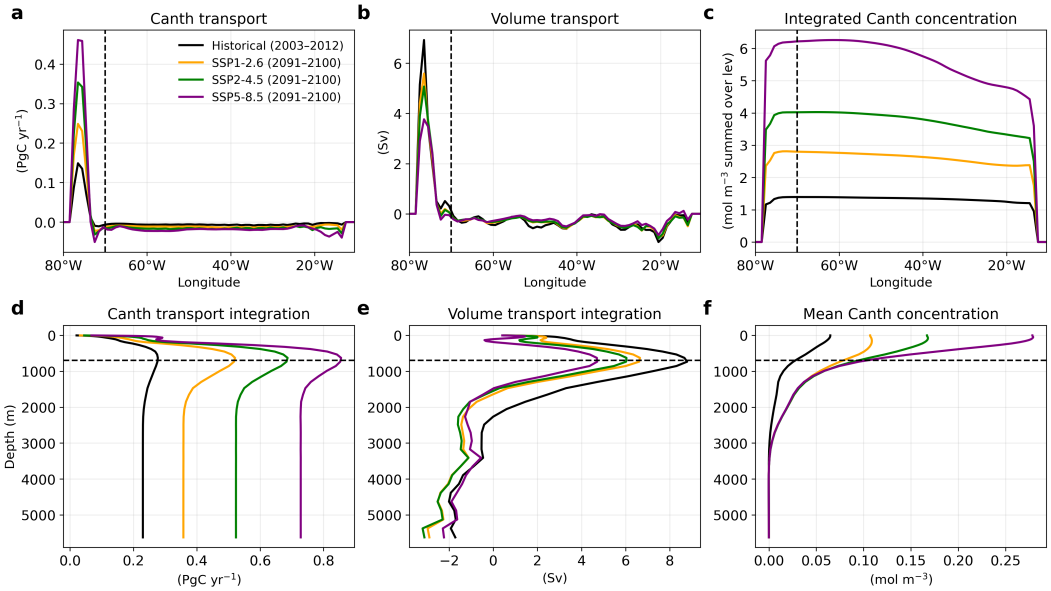

Figure 5. Spatial and vertical structure of C_{anth} transport at the RAPID 26°N section under historical and future climate conditions. Results are shown for the historical period 2004–2014 (black) and for the end of this century 2090–2100: SSP1-2.6 (orange), SSP2-4.5 (green), and SSP5-8.5 (purple). (a) Longitudinal distribution of depth-integrated C_{anth} transport. (b) Longitudinal distribution of depth-integrated net volume transport. (c) Longitudinal distribution of vertically integrated C_{anth} concentration. In (a–c), the vertical dashed black line indicates the boundary between the western boundary current (WBC) and the non-WBC region (approximately 80°W–70°W), defined based on the longitude where the depth-integrated volume transport changes sign from positive to non-positive. (d) Vertically cumulative C_{anth} transport integrated from the surface down to each depth, shown as zonal means. (e) Vertically cumulative volume transport integrated from the surface down to each depth, shown as zonal means. (f) Vertical profile of zonal-mean C_{anth} concentration. In (d–f), the horizontal dashed black line marks 700 m, corresponding to the depth at which the cumulative C_{anth} transport and cumulative volume transport reach their maxima.

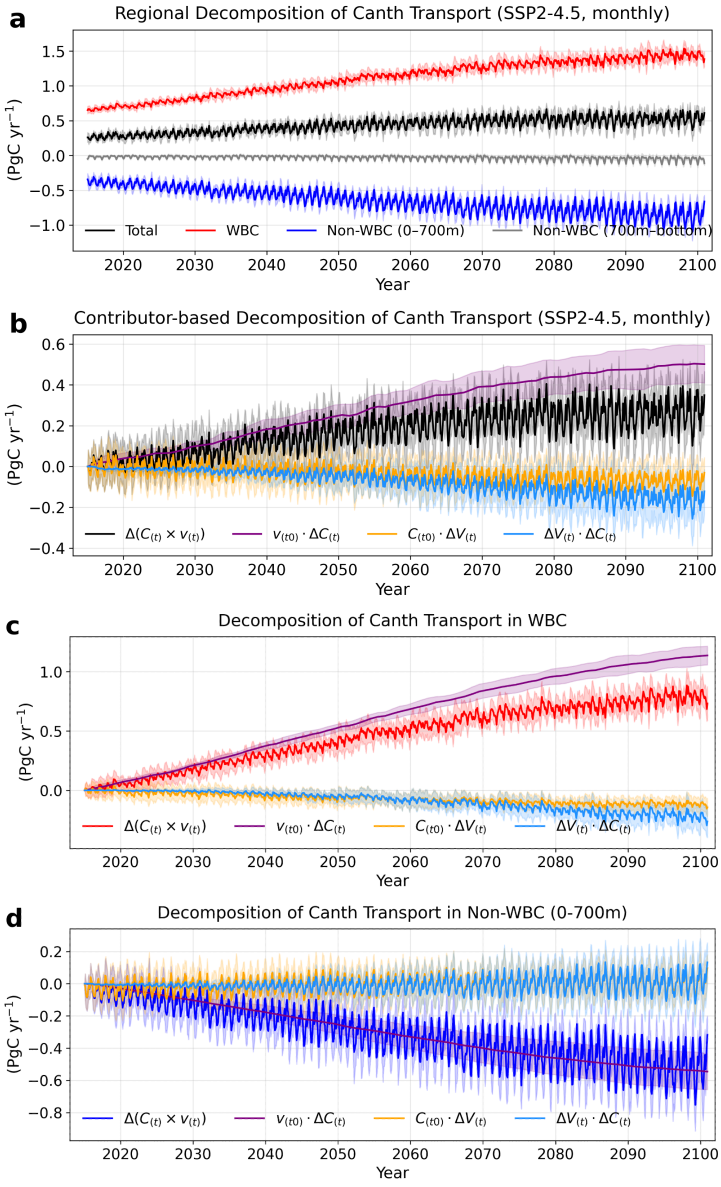

Figure 6. Decomposition of C_{anth} transport at the RAPID 26°N section under the SSP2-4.5 scenario. (a) is the regional decomposition of total C_{anth} transport (balck line) into contributions from the western boundary current (WBC; red), the upper interior ocean (0-700 m; dark blue), and the deep interior ocean (700 m-bottom; grey). Shaded regions indicate the inter-member spread (± 1 standard deviation) across the ensemble. (b) Contributor-based decomposition of total C_{anth} transport into four terms: $\Delta C_{(t)} \times V_{(t)}$ (black), $V_{(t0)} \cdot \Delta C_{(t)}$ (purple), $C_{(t0)} \cdot \Delta V_{(t)}$ (orange), and $\Delta V_{(t)} \cdot \Delta C_{(t)}$ (light blue), where t_0 denotes the initial reference state (JAN 2004) and Δ indicates anomalies relative to t_0. (c) Same decomposition as in (b), but restricted to the WBC region. (d) Same decomposition as in (b), but for the interior upper ocean (Non-WBC, 0-700 m). Results for SSP1-2.6 and SSP5-8.5 are shown in Figures S6 and S7, respectively.

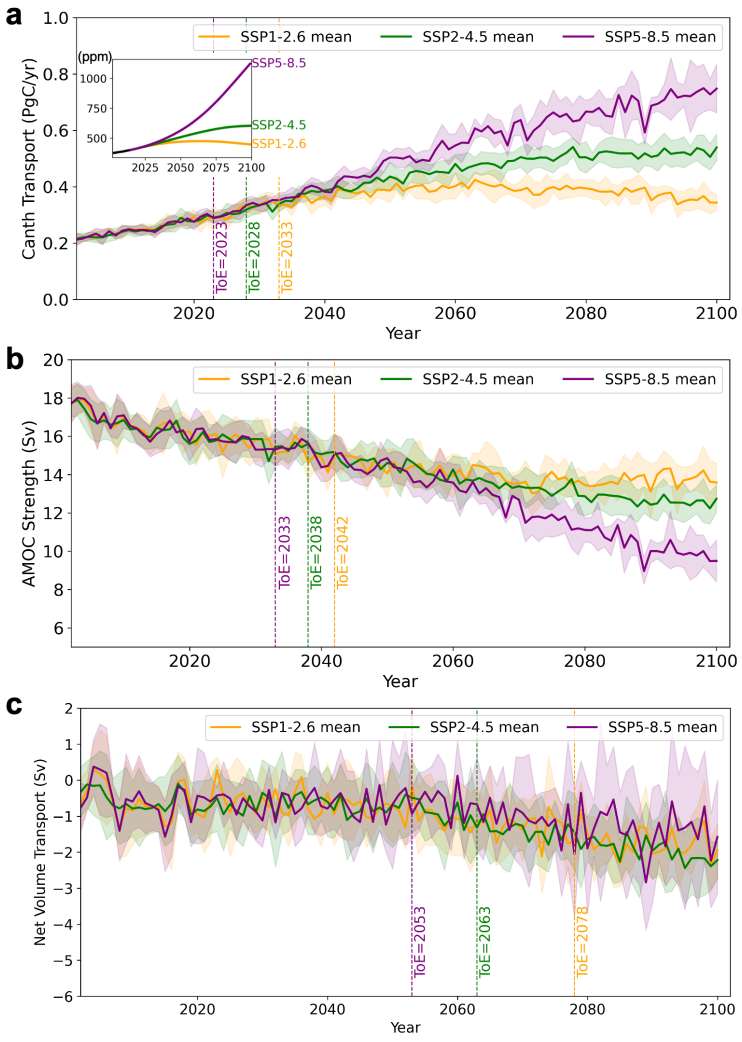

Figure 7. Time of emergence (ToE) of anthropogenic signals at the RAPID 26.5°N section. The ToE is defined as the earliest year at which the forced signal exceeds two standard deviations of internal variability for at least five consecutive years, indicating a robust detection of the anthropogenic signal. Solid lines represent the ensemble mean under SSP1-2.6 (orange), SSP2-4.5 (green), and SSP5-8.5 (purple), with shading indicating the inter-member spread (±1 standard deviation). (a) C_{anth} transport integrated over RAPID. Vertical dashed lines mark the estimated ToE years of 2033 (SSP1-2.6), 2028 (SSP2-4.5), and 2023 (SSP5-8.5). The inset shows the corresponding atmospheric CO_2 trajectories under each SSP scenario. Same as (a), (b) represent AMOC strength at RAPID. Vertical dashed lines indicate the corresponding ToE estimates (2042 for SSP1-2.6, 2038 for SSP2-4.5, and 2033 for SSP5-8.5). (c) represent the net volume transport across the RAPID section and their ToE year (2078 for SSP1-2.6, 2063 for SSP2-4.5, and 2053 for SSP5-8.5).

Supporting Information[0.5cm]
Future Strengthening of North Atlantic Anthropogenic Carbon Transport Despite AMOC Weakening[0.5cm]

Ce Bian, Galen A. McKinley, Peter J. Brown, and Elaine L. McDonagh

Contents of this file

Figures S1–S7 and Table S1.

Supplementary Figures

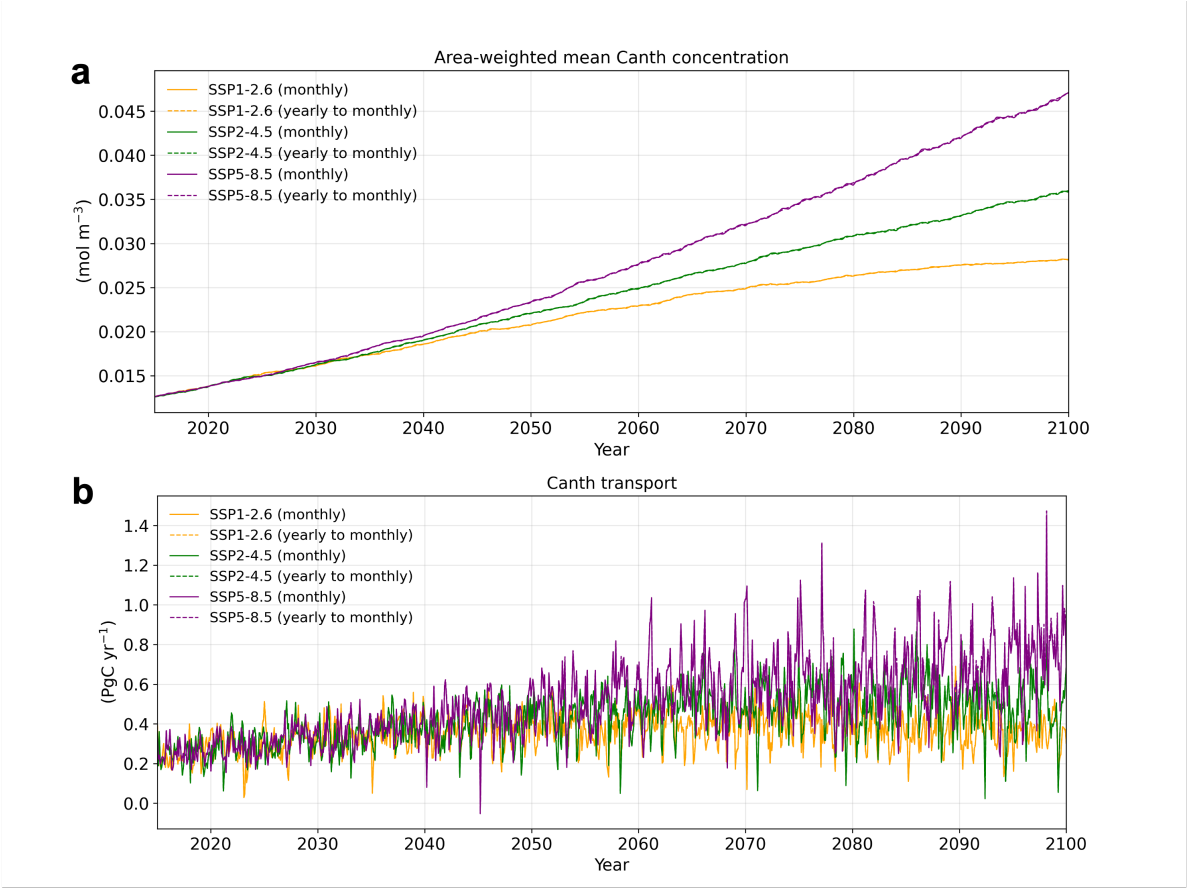

Figure S1. Comparison between monthly and reconstructed monthly results based on yearly outputs from the CanESM experiment (r1i1p2f1). (a) Comparison of the direct monthly output of area-weighted mean C∗*anth* concentration (solid line) and monthly dataset interpolated from yearly output (dashed lines) under SSP1-2.6 (orange), SSP2-4.5 (green), and SSP5-8.5 (purple). (b) Same as (a), but for C∗*anth* transport. The two estimates are practically indistinguishable.

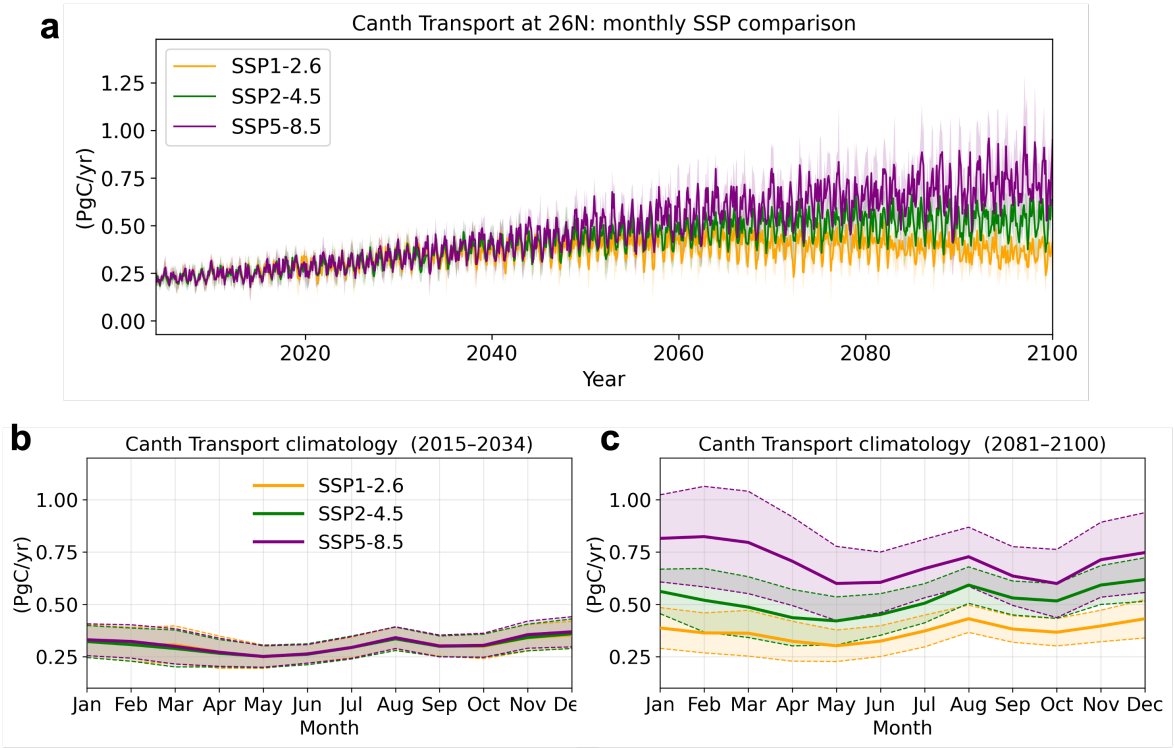

Figure S2. Monthly variability and seasonal structure of C∗*anth* transport at the RAPID 26°N section under different emission scenarios. (a) Time series of monthly C∗*anth* transport under SSP1-2.6 (orange), SSP2-4.5 (green), and SSP5-8.5 (purple) for 2015–2100. Solid lines represent the ensemble mean, and shaded regions denote the inter-member spread (±1 standard deviation). (b) Monthly climatology of C_{anth} transport for the early period (2015–2034). Solid lines indicate the climatological mean for each scenario, and dashed lines represent the corresponding inter-member spread (±1 standard deviation). (c) Same as (b), but for the late period (2081–2100).

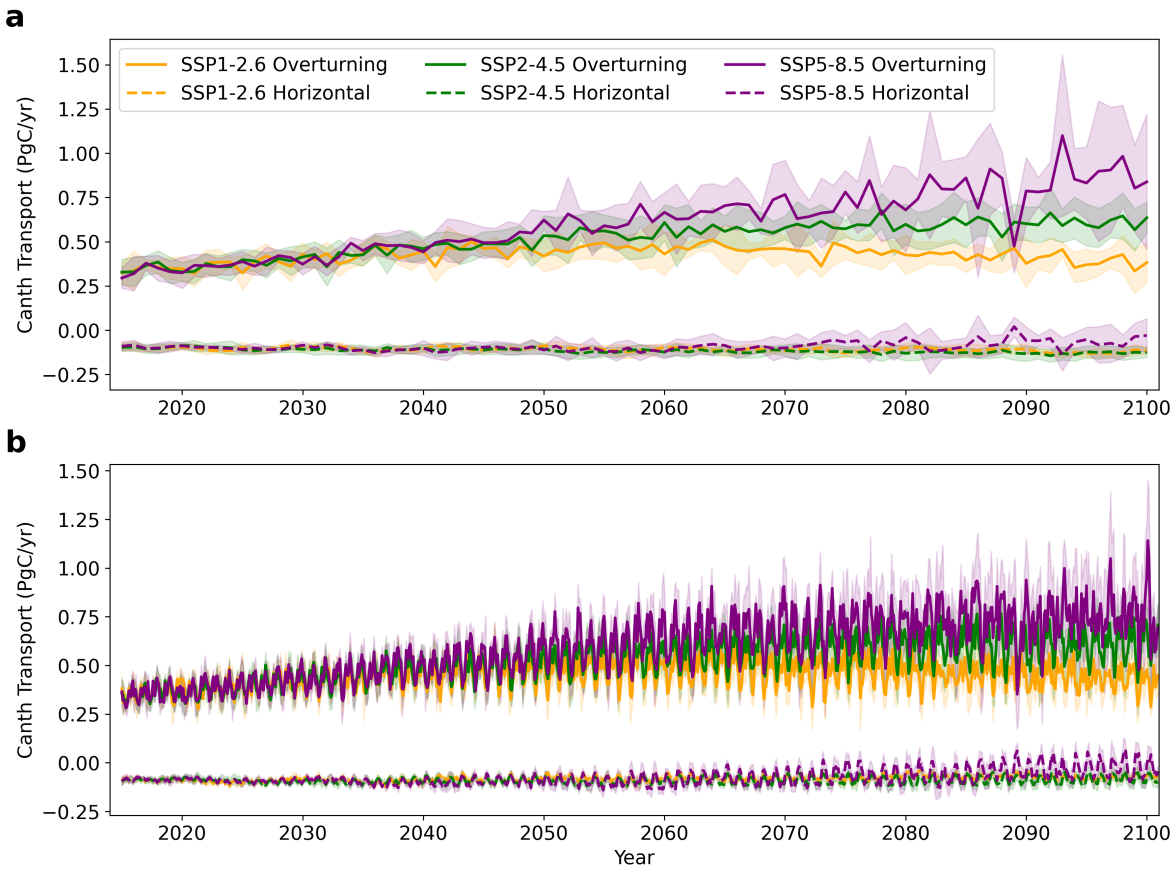

Figure S3. Decomposition of C∗*anth* transport into overturning and horizontal components across the RAPID 26.5°N section under future emission scenarios. (a) Annual mean C∗*anth* transport at the RAPID section for SSP1-2.6 (orange), SSP2-4.5 (green), and SSP5-8.5 (purple). Solid lines denote the overturning component, while dashed lines represent the horizontal component. Shading indicates the inter-member standard deviation. (b) Monthly C_{anth} transport and its decomposition for the same scenarios.

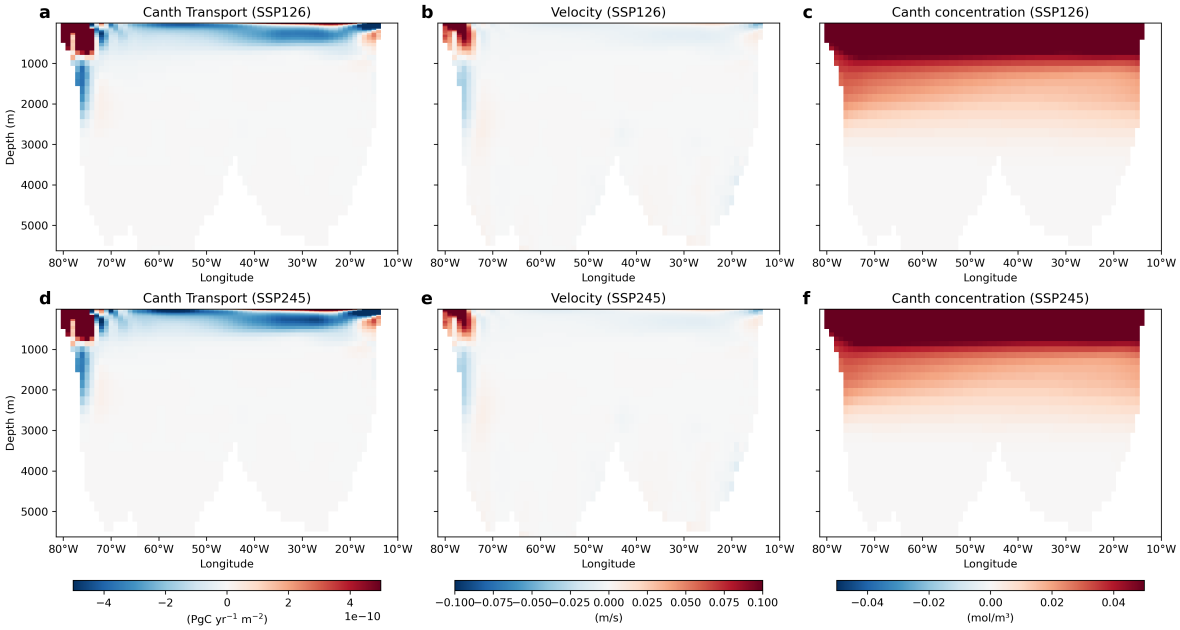

Figure S4. Spatial structure of C∗*anth* transport and its drivers across the RAPID 26.5°N section under SSP1-2.6 and SSP2-4.5 scenarios. (a–c) Time-mean zonal–vertical sections of C∗*anth* transport, meridional velocity (v), and C_{anth} concentration for SSP1-2.6 (2015–2100). (d–f) Same as (a–c), but for SSP2-4.5 (2015–2100). Red shading indicates positive values. Results for SSP5-8.5 are shown in Figure 4 of the main text.

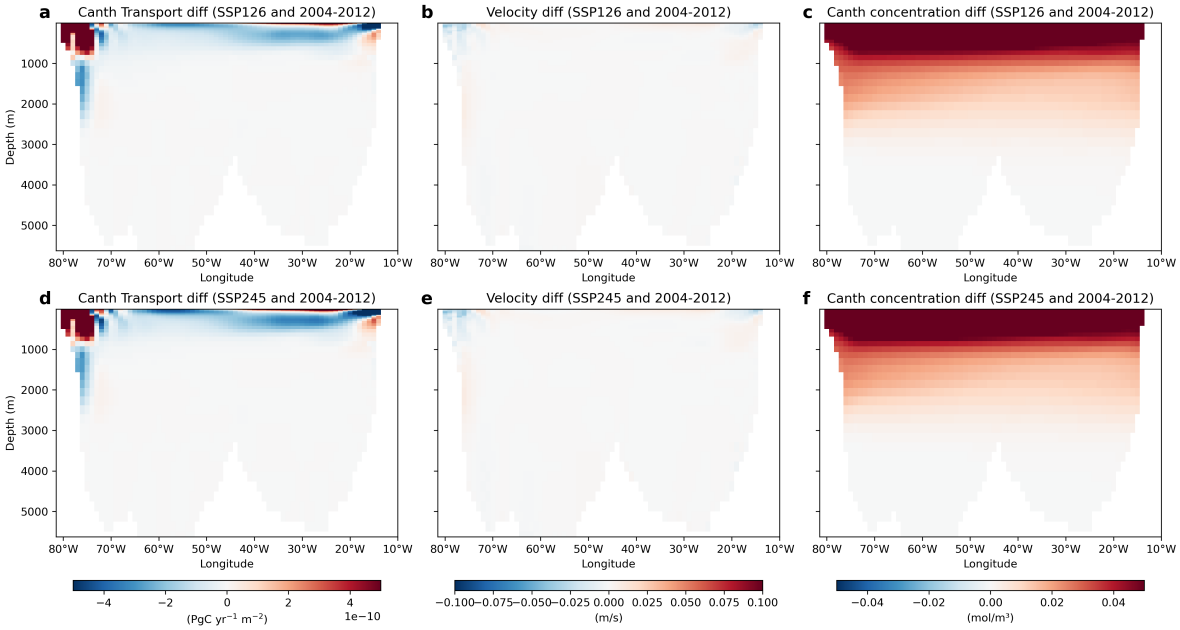

Figure S5. Changes in C∗*anth* transport and its drivers between historical and future scenarios. (a–c) Differences between SSP1-2.6 and the historical period (2004–2012) for C∗*anth* transport, velocity, and C_{anth} concentration. (d–f) Same as (a–c), but for SSP2-4.5. Red shading indicates an increase in the future scenarios relative to the historical mean. Results for SSP5-8.5 are shown in Figure 4 of the main text.

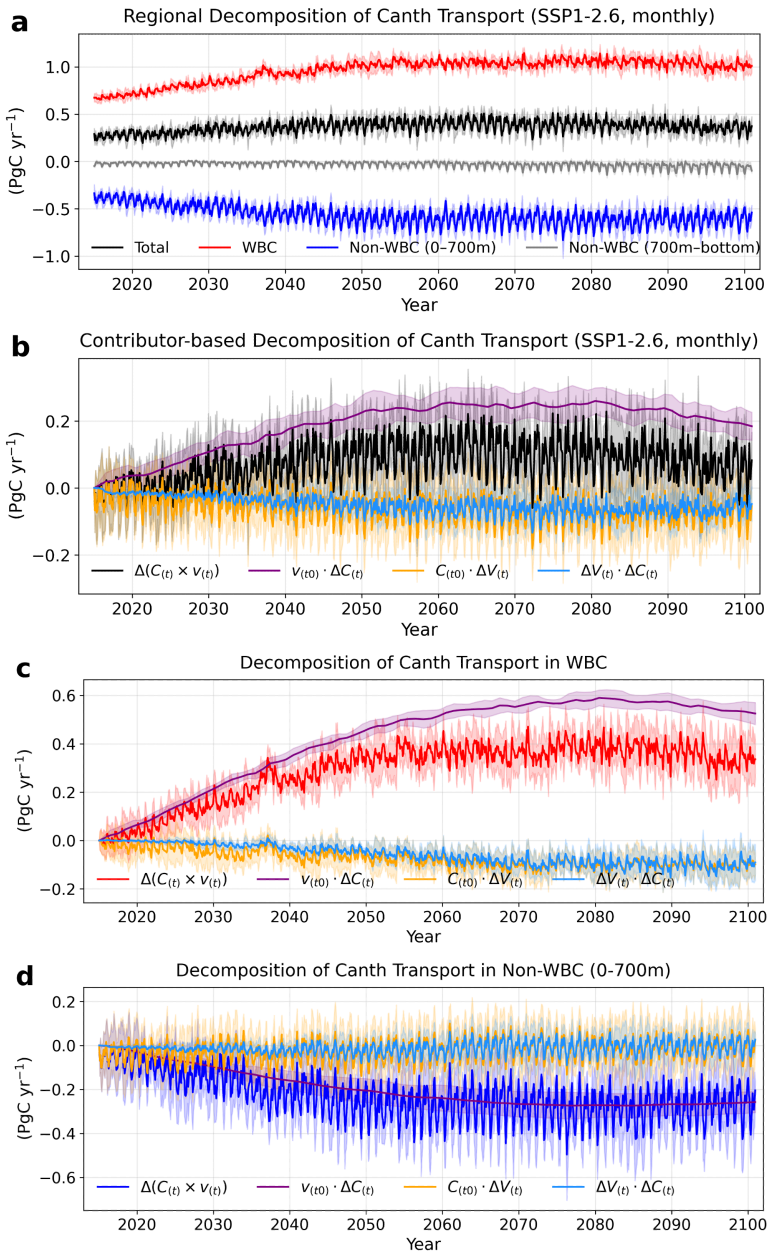

Figure S6. Decomposition of C_{anth} transport changes under the SSP1-2.6 scenario.

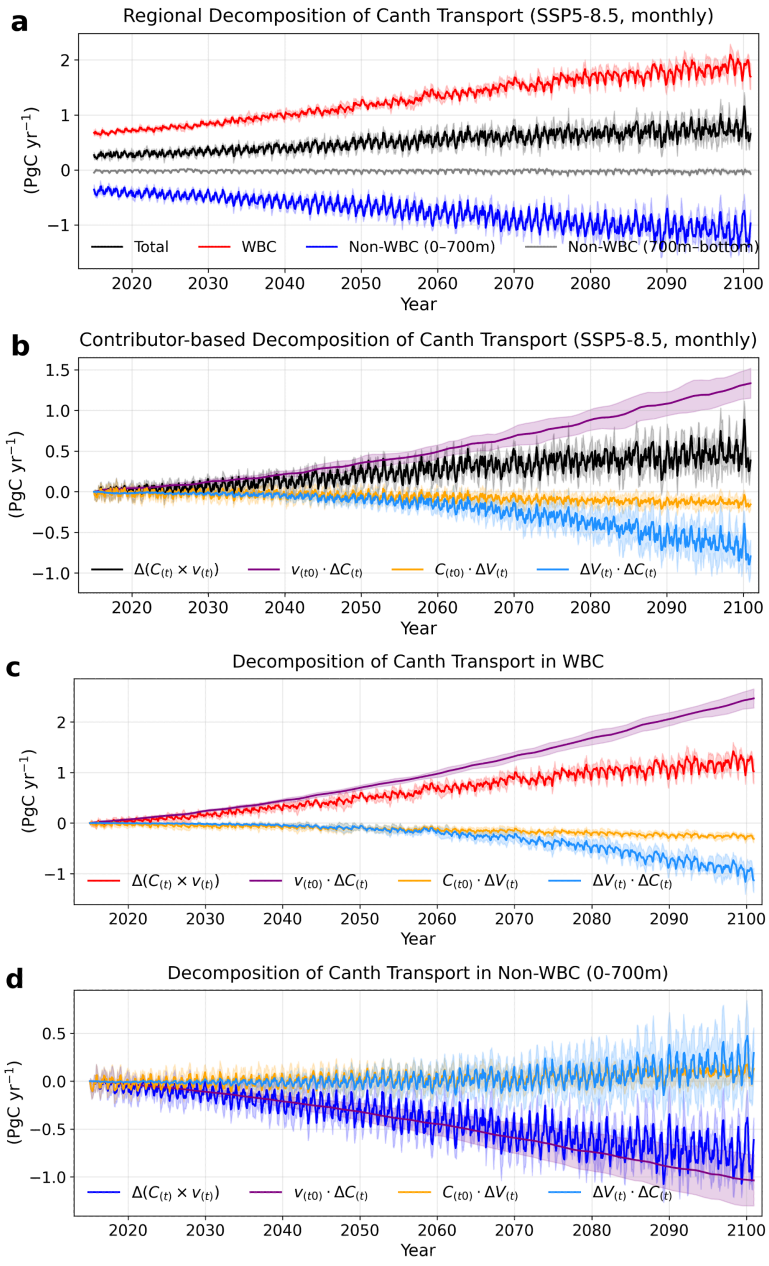

Figure S7. Decomposition of C_{anth} transport changes under the SSP5-8.5 scenario. Same as Figure 6, but for SSP5-8.5 during 2015–2100 and with different vertical scales.

Supplementary Table

Table S1. Data availability and ensemble selection for CMIP6 simulations.

This table summarizes the availability of velocity (vo), dissolved inorganic carbon (dissic), and natural dissolved inorganic carbon (dissicnat) across the historical and SSP experiments, including their temporal resolutions (monthly, Omon; yearly, Oyr) and ensemble members. Because the overlap of monthly carbon variables across ensemble members is limited, annual dissic and dissicnat outputs are used to reconstruct anthropogenic carbon (C_{anth}), which is then temporally interpolated to monthly resolution. The final ensemble used in this study is defined based on the intersection of available velocity and carbon fields, ensuring consistency across variables and experiments.

Experiment	Variable	Temporal resolution	Matching experiments
Historical	vo	Omon (55)	Omon (55)
Historical	dissic & dissicnat	Omon (55)	
SSP1-2.6	vo	Omon (10)	Omon (by Oyr interp, 7)
SSP1-2.6	dissic & dissicnat	Omon (1), Oyr (13)	
SSP2-4.5	vo	Omon (19)	Omon (by Oyr interp, 14)
SSP2-4.5	dissic & dissicnat	Omon (1), Oyr (15)	
SSP5-8.5	vo	Omon (10)	Omon (by Oyr interp, 7)
SSP5-8.5	dissic & dissicnat	Omon (1), Oyr (13)	